Tectonophysics 631 (2014) 50–64

Contents lists available at ScienceDirect

Tectonophysics

journal homepage: www.elsevier.com/locate/tecto

Influence of lithospheric mantle stratification on craton extension: Insight from two-dimensional thermo-mechanical modeling

Jie Liao *, Taras Gerya

Geophysical Fluid Dynamics, Institute of Geophysics, ETH Zurich, Sonneggstrasse 5, CH-8092 Zurich, Switzerland

ARTICLE INFO

Article history:
Received 16 October 2013
Received in revised form 9 January 2014
Accepted 13 January 2014
Available online 24 January 2014

Keywords:
Stratified cratonic lithosphere
Weak mantle layer
Craton extension
Thermo-mechanical numerical modeling

ABSTRACT

Lithospheric mantle stratification is a common feature in cratonic areas which has been demonstrated by geophysical and geochemical studies. The influence of lithospheric mantle stratification during craton evolution remains poorly understood. We use a 2D thermo-mechanical coupled numerical model to study the influence of stratified lithospheric mantle on craton extension. A rheologically weak layer representing hydrated and/or metasomatized composition is implemented in the lithospheric mantle. Our results show that the weak mantle layer changes the dynamics of lithospheric extension by enhancing the deformation of the overlying mantle and crust and inhibiting deformation of the underlying mantle. The thickness and depth of the weak layer determines two deformation patterns: 1) narrow mantle necking favored by shallow and thin weak layer, and 2) widespread mantle necking favored by deep and thick weak layer. High Moho temperatures also promote the formation of widespread mantle necking in the model with a weak mantle layer. Both shear heating and plastic strain weakening can enhance deformation and promote asymmetric extension. Modeling results are compared with North China and North Atlantic cratons. Our work indicates that although the presence of a weak layer may not be sufficient to initiate craton deformation, it enhances deformation by lowering the required extensional plate boundary force.

1. Introduction

Cratons are continental areas on the Earth which are stabilized since the Archean. Geodynamic modeling studies show that positive chemical buoyancy, high viscosity, high yield strength and large thickness of cratonic root are key factors that ensure the long-term craton stability under the condition of an ongoing mantle convection, although each factor may be individually insufficient to account for the craton stability (Cooper et al., 2006; Gerya, 2014; Lenardic and Moresi, 1999; Lenardic et al., 2000, 2003; O'Neill et al., 2008; Yoshida, 2012). In addition to the intrinsic cratonic features, relatively weak zones on craton margins such as the weak zones surrounding Tanzanian Craton and Siberian Craton (Chemenda et al., 2002; Vauchez et al., 1997), play a role in protecting craton from destruction (Lenardic et al., 2000; Lenardic et al., 2003; Yoshida, 2012), because deformation mainly localizes in the weak zone areas (Dunbar and Sawyer, 1988). Conditions required for craton stability in the past (Archean) and in the present day are different, as the mantle was hotter and more energetic in the past. Modeling from O'Neill et al. (2008) shows that with a higher mantle heat production, a craton can maintain stability even longer, as high temperatures reduce the mantle viscosity which increases the viscosity contrast between cratonic root and the surrounding mantle. Although most cratons observed today are stable, there are some exceptions, such as the North China Craton (Menzies et al., 2007), North Atlantic Craton (Tappe et al., 2007), which have experienced dramatic deformation (for instance the Precambrian lithospheric mantle has been totally renewed since Mesozoic in the North China Craton). The reasons why cratons undergo destruction are even more enigmatic. How cratons maintain stability, or undergo destruction, remains a frequently debated topic.

A common characteristic of the cratonic lithosphere–mantle stratification has been recently widely detected by geophysical and geochemical studies. These observations challenge previous numerical studies that assumed homogeneous lithospheric mantle structure under cratons. The mid-lithospheric boundary has been imaged globally and locally under cratonic regions by using different seismic tools (Table 1). The low velocity zone below 100 km depth in continental mantle is revealed by the so-called "8 degree discontinuity"—the strong, scattered reflections beyond 8° (700–900 km) offset in numerous continental high-resolution, long-range seismic profiles. Based on the global study of Ps receiver functions, Rychert and Shearer (2009) detected a negative sharp velocity interface at depth of 95 ± 4 km beneath cratonic regions globally, which is too sharp and too shallow to be the cratonic lithosphere–asthenosphere boundary (LAB) (Gung et al., 2003; Romanowicz, 2009). This mid-lithospheric interface is also revealed at the depth of 100–150 km under North American Craton by azimuthal anisotropy studies (Yuan and Romanowicz, 2010), corresponding to the maximum direction gradient of the fast axis of azimuthal anisotropy and the minimum in azimuthal anisotropy amplitude. Ps and Sp

* Corresponding author.
E-mail address: jie.liao@erdw.ethz.ch (J. Liao).

0040-1951/$ – see front matter © 2014 Elsevier B.V. All rights reserved.
http://dx.doi.org/10.1016/j.tecto.2014.01.020

Table 1
Seismic evidences of mid-lithospheric boundary in cratonic regions.

Ref.[a]	Method	Evidence	Depth	Regions	Possible reason(s)
1	Seismic arrival time	Scattered seismic arrivals beyond ~8° offset	~100 km	Globally	Melts
2	RF[b] (*Ps*)	Sharp velocity drop (6%)	~95 km	Globally	Radial anisotropy decrease
3	S wave velocity	Sharp velocity drop	~100 km	Globally	Remnant structure
4	Azimuthal anisotropy	Change of direction of azimuthal anisotropy	100–150 km	North America	Compositional layers
5	RF (*Sp* and *Ps*)	Negative *Sp* phase	59–113 km	North America	Mentioned above

[a] 1 Thybo, (2006) and Thybo and Perchuc (1997), 2 Rychert and Shearer (2009), 3 Cammarano and Romanowicz (2007), Mercier et al. (2008), and Romanowicz (2009), 4 Yuan and Romanowicz (2010), 5 Abt et al. (2010).
[b] Receiver function.

receiver function studies proved the existence of this internal boundary (at depths of 59–113 km) overlying a low velocity zone in the cratonic lithosphere in North America (Abt et al., 2010). Geochemical studies revealed the layered structure in lithospheric mantle underneath cratons based on the xenolith studies, for instance, the chemically-layered structure across the whole North American Craton (the base boundary of the highly depleted upper layer is in agreement with the mid-lithospheric boundary revealed by Yuan and Romanowicz (2010) and Griffin et al. (2004)), the two-chemically-layered structure in the Archean Slave craton (depleted upper layer and refertilized lower layer) (Kopylova and Russell, 2000), and the three-chemically-layered structure in the Karelian craton in Finland (highly depleted upper layer, intermediate modified middle layer, highly refertilized lower layer) (Peltonen and Brügmann, 2006).

The exact nature of the mid-lithospheric boundary detected by seismic studies is complex, and several possible explanations are proposed (Fig. 1). The presence of melts is a favorite explanation for the global occurrence of the low velocity zone in lithospheric mantle, since a small amount of melts can significantly decrease seismic velocities (Karato and Jung, 1998; Thybo, 2006). However, the presence of melts in cratonic lithosphere is debated, because cratonic lithosphere is too cold to interact with the mantle solidus (Abt et al., 2010; Griffin et al., 2004). Radial anisotropy variation with depth (Nettles and Dziewonski, 2007) is proposed by Rychert and Shearer (2009) to explain the mid-lithospheric boundary that they observed by receiver function (red dashed line in Fig. 1b). One scenario of craton formation is that cratonic root is formed by thrust stacking during continental collision (Gray and Pysklywec, 2010). The interface/shear zone between

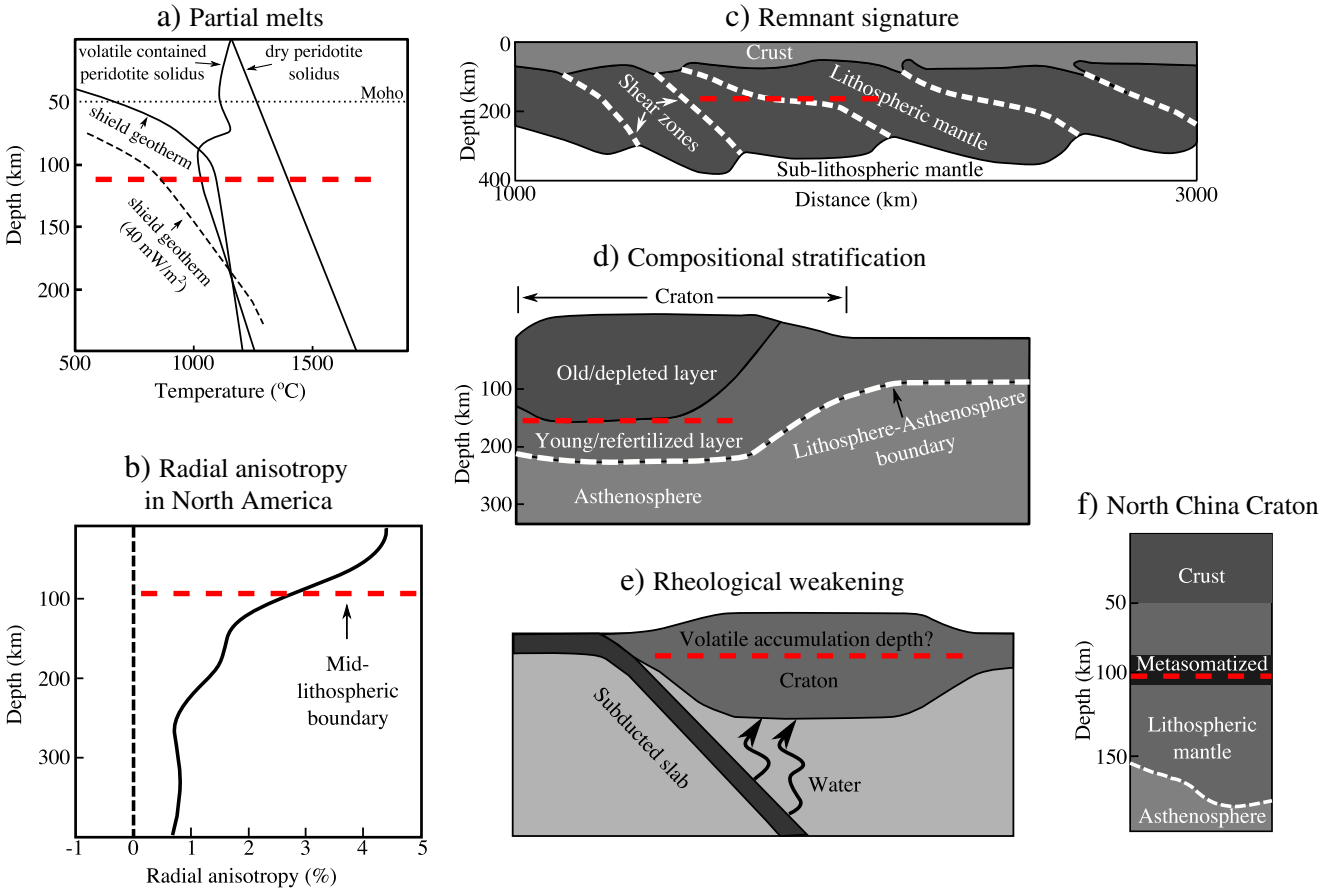

Fig. 1. Possible mechanisms for mid-lithospheric boundary in cratonic areas. (a) Partial melting generation due to the intersection of mantle solidus and geotherms (modified after Thybo and Perchuc, 1997). Dashed geotherm is modified after Tappe et al. (2007). (b) Decrease in radial anisotropy with depth (modified after Nettles and Dziewonski, 2007). (c) Remnant structure preserved during craton formation through continental collision/thrust stacking (modified after Gray and Pysklywec, 2010). (d) Sketch showing compositional stratification in the North American craton (modified after Yuan and Romanowicz, 2010). (e) Sketch showing rheological weakening due to re-hydration where water is released from subducting slabs (modified after Lee et al., 2011). (f) Sketch showing the possibility of a metasomatized layer in North China craton before its destruction (modified after Xu, 2001). The red dashed lines show the possible depth of mid-lithospheric boundary in cratons.

the stacked layers (Fig. 1c) is proposed as one possible origin for the mid-lithospheric boundary (Romanowicz, 2009). Bulk composition changes of the lithosphere (Fig. 1d) could be responsible for the mid-lithospheric boundary detected in the North American craton (Yuan and Romanowicz, 2010), where the upper layer is old and depleted (corresponds to the original part of cratonic root), while the lower layer is relatively young (corresponds to refertilized composition). Water released from subducting slabs can rehydrate the overlying cratonic lithosphere (Lee et al., 2011). The ascending water (and other volatiles) is ponding potentially at the depth corresponding to the peak strength of the lithosphere (Fig. 1e) (Sleep, 2009), therefore a metasomatized layer is likely present in the cratonic lithosphere, such as proposed (Xu, 2001) for the North China craton (Fig. 1f).

The layered structure detected by geochemical studies is commonly regarded as the consequence of mantle re-fertilization such as metasomatism resulting from the interaction of mantle rocks with melts and/or fluids either from subducting plates, or from magmatic intrusions (Griffin et al., 2003, 2009). Lithospheric strength can be dramatically reduced if metasomatism occurs over wide areas in the mantle (Carlson et al., 2005; Lee et al., 2011). In addition, re-hydration by water released from subducting slabs can significantly reduce the effective viscosity of cratonic lithosphere (Lee et al., 2011). The work done by Wang (2010) suggests strongly heterogeneous water distribution in the olivine from the continental upper mantle (0–170 ppm H_2O), which may result in local enhancement of the lithospheric deformation driven by relatively weak wet olivine rheology.

Only a few studies take into account the influence of lithospheric mantle stratification on craton evolution. O'Neill et al. (2010) studied the effects of mantle layered structure on craton evolution numerically, by imposing a relatively weak mantle layer (representing a metasomatized layer) with different geometries at the base of the cratonic lithosphere. Although the weak layer influences the lithosphere–asthenosphere coupling, it does not systematically affect the stress regime. In this study, we investigate the extensional dynamics of cratonic lithosphere containing a rheologically weak layer inside the lithospheric mantle (hereby layered model), and compare results to the extension of a homogeneous model without a weak layer in the mantle lithosphere (hereby homogeneous model). Since detailed comparison of differences in lithospheric extension styles between homogenous and layered models has been previously examined (Liao et al., 2013), here we mainly focus on studying various layered models and investigate the influence of depth and thickness of the weak layer, Moho temperature, and weakening effects (shear heating and plastic strain weakening) on lithospheric extension, and compare the modeling results to natural examples.

2. Methodology

2.1. Governing equations

The 2D thermo-mechanical coupled numerical code I2ELVIS (Gerya and Yuen, 2007) based on finite-differences and marker-in-cell techniques is used to solve the mass, momentum and energy conservation equations for an incompressible media:

$$\frac{\partial v_i}{\partial x_i} = 0 \tag{1}$$

$$\frac{\partial \sigma_{ij}}{\partial x_j} - \frac{\partial P_i}{\partial x_i} = -\rho g_i \tag{2}$$

$$\rho C_p \left(\frac{\partial T}{\partial t} + v_i \frac{\partial T}{\partial x_i}\right) = \frac{\partial}{\partial x_i}\left(k \frac{\partial T}{\partial x_i}\right) + H_r + H_s + H_a \tag{3}$$

where v is velocity, σ the deviatoric stress tensor, P the total pressure (mean normal stress), ρ the density, g the gravitational acceleration, C_p the heat capacity, T the temperature, k the thermal conductivity, H_r the radioactive heating, $H_s = \sigma_{ij}\left(\dot{\epsilon}_{ij} - \dot{\epsilon}_{ij}^{ela}\right)$ the shear heating (stress tensor multiply the non-elastic strain rate), and $H_a = T\alpha\frac{Dp}{Dt}$ the adiabatic heating. The Einstein notation is used for the indexes i and j, which denote spatial directions $i = (x, y)$ and $j = (x, y)$ in 2D.

2.2. Rock rheology implementation

Visco-elasto-plastic rheology is implemented based on the assumption that viscous, elastic and plastic deformations are happening under the same deviatoric stress (Gerya, 2010), therefore, the total strain rate can be represented by the summation of the three parts:

$$\dot{\epsilon}_{ij} = \dot{\epsilon}_{ij}^{vis} + \dot{\epsilon}_{ij}^{ela} + \dot{\epsilon}_{ij}^{pla} = \frac{1}{2\eta}\sigma_{ij} + \frac{1}{2\mu}\frac{D\sigma_{ij}}{Dt} + \frac{\chi}{2\sigma_{II}}\sigma_{ij} \tag{4}$$

where $\dot{\epsilon}_{ij}^{vis}$, $\dot{\epsilon}_{ij}^{ela}$, and $\dot{\epsilon}_{ij}^{pla}$ denote viscous, elastic and plastic strain rates, respectively. μ is shear modulus, $\frac{D\sigma_{ij}}{Dt}$ the objective derivative, χ the plastic multiplier, $\sigma_{II} = \left(\frac{1}{2}\sigma_{ij}\sigma_{ij}\right)^{\frac{1}{2}}$ the second invariant of stress, and η the effective creep viscosity which represents the competition between diffusion and dislocation creeps (Ranalli, 1995): $\eta = 1/(1/\eta_{diff} + 1/\eta_{disl})$, where η_{diff} and η_{disl} are computed as:

$$\eta_{diff} = \frac{1}{2}A_d {\sigma_{crit}}^{1-n} exp\left(\frac{PV_a + E_a}{RT}\right) \tag{5}$$

$$\eta_{disl} = \frac{1}{2}A_d {\sigma_{II}}^{1-n} exp\left(\frac{PV_a + E_a}{RT}\right) \tag{6}$$

where A_d is the pre-factor, n the stress exponent, V_a the activation volume, E_a the activation energy, R the gas constant, and $\sigma_{crit} = 10^4$ Pa is the transition stress from diffusion to dislocation creep (Turcotte and Schubert, 2002). Although diffusion creep is happening all the time, dislocation creep dominates the deformation. Once when the yielding criterion is reached $\sigma_{II} >= \sigma_y$, effective viscosity is limited by the plastic yielding stress:

$$\eta = \frac{\sigma_y}{2\dot{\epsilon}_{II}} = \frac{C_0 cos(arcsin(\phi)) + P\phi}{2\dot{\epsilon}_{II}} \tag{7}$$

where σ_y is the plastic yielding stress, C_0 the cohesion (the residual strength of rock when pressure is zero), ϕ the coefficient of internal friction, $\dot{\epsilon}_{II}$ the second invariant of strain rate. At sufficient high stress and low temperature, Peierls creep takes over from dislocation creep. In our model, the Peierls creep is implemented to constrain the plastic yield stress, and therefore it also constrains the effective viscosity. Constitution equation of Peierls creep can be expressed in such manner (Katayama and Karato, 2008):

$$\dot{\epsilon}_{II} = A_{Pei}\sigma_{II}^2 exp\left\{-\frac{PV_a + E_a}{RT}\left[1 - \left(\frac{\sigma_{II}}{\sigma_{Pei}}\right)^m\right]^n\right\} \tag{8}$$

where $\sigma_{Pei} = 9.1 \times 10^9$ Pa, $A_{Pei} = 6.3 \times 10^{-5}$ Pa^{-2} s^{-1}, $m = 1$, $n = 2$ are experimentally determined parameters (Katayama and Karato, 2008).

Volumetric fraction of melt M increases linearly with temperature for a certain pressure (Gerya and Yuen, 2003b): $M = 0$ for $T \le T_{solidus}$, $M = 1$ for $T \ge T_{liquidus}$ and $M = \frac{T - T_{solidus}}{T_{liquidus} - T_{solidus}}$ for $T_{solidus} < T < T_{liquidus}$, where $T_{solidus}$ and $T_{liquidus}$ are the solidus and liquidus of a considered rock, respectively (Table 2), and they are pressure-dependent. We use highly simplified rheological model for partially molten rocks according to which rocks with $M < 0.1$ are assigned by solid state flow law, whereas rocks with $M > 0.1$ are assigned by lower cutoff viscosity of 10^{18} Pa s. Besides, no melt extraction is simulated in our models. The melt fraction M also influences the effective density (ρ_{eff}) of partial melting rocks: $\rho_{eff} = \rho_{solid}(1 - M) + \rho_{molten}M$, where ρ_{solid} and ρ_{molten} are the densities of

Table 2
Temperature-and pressure-dependent parameters used in the numerical experiments.

	$T_{solidus}$ (K)	Ref.[a]
Crust	$889 + 536.6/(0.03P + 1.609) + 18.21/(0.03P + 1.609)^2$ at $P < 1200$ MPa, $831 + 0.06P$ at $P \geq 1200$ MPa	1,2
Mantle	$1393.811 + 0.132899P - 5.104 \times 10^{6}P^2$ at $P < 10{,}000$ MPa, $2212.4 + 0.030819\,(P - 10^4)$ at $P \geq 10{,}000$ MPa	3
Weak zone	$1239.8 + 1493.0/(0.03P + 9.701)$ at $P < 2400$ MPa, $1266.3 - 0.011844P + 3.5 \times 10^{6}P^2$ at $P \geq 2400$ MPa	4
	$T_{liquids}$ (K)	
Crust	$1262.0 + 0.09P$[b]	1
Mantle	$2073.15 + 0.114P$	5
Weak zone	$2073.15 + 0.114P$	5
	k (W m^{-1} K^{-1})	
Crust	$[1.18 + 474/(T + 77)]\exp(0.00004P)$	6
mantle	$[0.73 + 1293/(T + 77)]\exp(0.00004P)$	6
Weak zone	$[0.73 + 1293/(T + 77)]\exp(0.00004P)$	6

[a] 1 Johannes (1985)), 2 Poli and Schmidt (2002), 3 Hirschmann (2000), 4 Schmidt and Poli (1998), 5 Hess (1989), 6 Clauser and Huenges (1995).
[b] Pressure in unit of MPa.

solid and molten rocks, respectively. Rock density itself is also pressure and temperature dependent: $\rho = \rho_r[1 + \beta(P - P_r)][1 - \alpha(T - T_r)]$, where ρ_r is the density of a given material at the reference pressure P_r (10^5 Pa) and temperature T_r (298.15 K), β and α are the compressibility and thermal expansion, respectively. Latent heating effect due to melting/crystallization equilibrium is included implicitly by increasing the effective heat capacity and thermal expansion in the energy conservation equation:

$$Cp_{eff} = CP + Q_L\left(\frac{\partial M}{\partial T}\right)_p \tag{9}$$

$$\alpha_{eff} = \alpha + \rho\frac{Q_L}{T}\left(\frac{\partial M}{\partial P}\right)_T \tag{10}$$

where Q_L is the latent heat. The material parameters are shown in Tables 2 and 3.

2.3. 2D model setup

2D numerical models are designed for studying craton extension with a stratified mantle lithosphere (Fig. 2). The dimension of the model box is 600×250 km (equivalent to 1201×501 nodes in a fully staggered 2D grid), and around 3 million Lagrangian markers are randomly distributed. The top layer is "sticky air", underlain by the homogeneous crustal layer and lithospheric mantle layer which is stratified by a hydrated mantle layer. A weak seed (2×2 km) using the same rock properties with the weak layer is imposed in the upper mantle, to initially generate a perturbation in the middle of the model domain. In order to investigate the difference caused by mantle layered structure, a homogeneous model which has the same model setup except for the homogeneous lithospheric mantle is employed.

The initial thermal state of the lithosphere is laterally uniform with zero horizontal heat flux across vertical boundaries. The crustal surface, Moho, and lithosphere–asthenosphere boundary (LAB) has an initial temperature of 0 °C, 450 °C and 1300 °C, respectively, and temperature linearly changes in the crust and mantle lithosphere. Higher initial Moho temperatures (600, 750 and 850 °C) also have been tested in this paper. Below the LAB, the asthenosphere has an adiabatic temperature gradient of 0.5 °C/km. A constant temperature (1320 °C) condition is used for the lower boundary of the models. We use high thermal conductivity of the sticky air ($k = 20$ W/m/K, $C_p = 100$ J/kg/K, $\rho = 1$ kg/m^3) and water ($k = 20$ W/m/K; $C_p = 3300$ J/kg/K, $\rho = 1000$ kg/m^3), which ensure small temperature variations in this layer and thus upper thermal boundary condition ($T = 273$ K) is efficiently transferred to the deforming upper surface of the crust (i.e. to the erosion/sedimentation surface). We also use subgrid thermal diffusion (Gerya and Yuen, 2003a) to ensure physical consistency between the nodal and marker thermal fields.

Prescribed velocity boundary condition is used. Extension velocities are prescribed on the left and right boundaries in the same magnitude but with opposite directions. The constant velocities on the upper and lower boundaries are computed on the basis of mass conservation:

$$v_{xl} = -v_{xr} \tag{11}$$

$$\frac{v_{xr} - v_{xl}}{l_x} + \frac{v_{yl} - v_{yu}}{l_y} = 0 \tag{12}$$

$$\frac{-v_{yl} + v_{yu}}{l_y} = \frac{v_{yu}}{l_a} \tag{13}$$

where v_{xl}, v_{xr}, v_{yu} and v_{yl} are the normal velocities on the left, right, upper and lower boundaries, respectively; l_x and l_y are the box

Table 3
Material parameters used in the numerical experiments.

Symbol[a]	Crust (wet quartzite)	Mantle (dry olivine)	Weak zone (wet olivine)	Ref. [b]
ρ (kg m^{-3})	2700	3300	3200	1
C_0 (Pa)	5×10^5	5×10^5	5×10^5	2
ϕ	0.4	0.6	0.6	2
E_α (J mol^{-1})	1.54×10^5	5.32×10^5	4.7×10^5	2
V_α (J Pa^{-1} mol^{-1})	0	0.8×10^{-5}	0.8×10^{-5}	2
A_D (Pa^n s)	1.97×10^{19}	3.98×10^{16}	5.01×10^{22}	2
n	2.3	3.5	4.0	2
H_r (μW m^{-3})	1.75	0.022	0.022	1
Q_L (kJ kg^{-1})	300	400	400	1,3

[a] The symbols are explained in the text. Other parameters (for all rocks): $C_P = 1000$ J kg^{-1} K^{-1}, $\alpha = 3 \times 10^{-5}$ K^{-1}, $\beta = 1 \times 10^{-5}$ MPa^{-1}.
[b] 1 Turcotte and Schubert, (2002), 2 Ranalli (1995), 3 Bittner and Schmeling (1995).

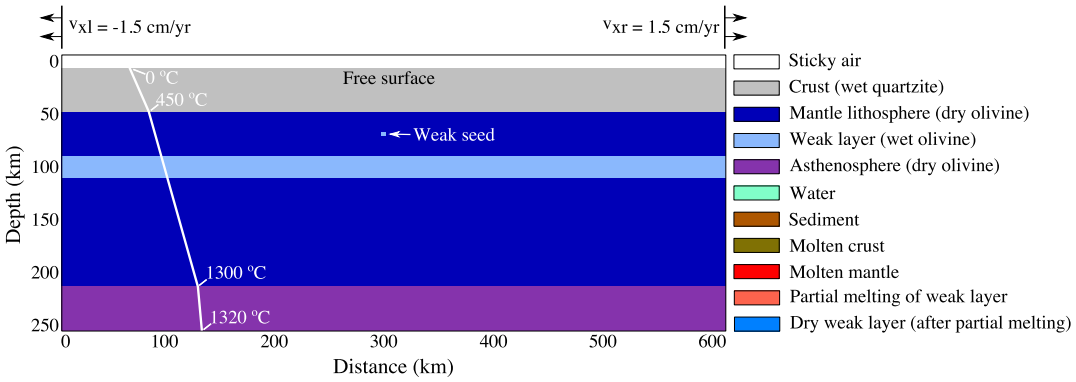

Fig. 2. Initial setup of the layered model. The top layer in the model is 10 km thick sticky air (which approximates the upper surface of the crust as a free surface), underlain by a 40 km thick homogeneous crustal layer. Mantle lithosphere is 160 km thick, stratified by a weak layer. The depth and thickness of the weak layer varies in different models. A weak seed is used to localize initial deformation in the center of the model (Huismans and Beaumont, 2011). Initial temperature increases linearly in the crust and mantle lithosphere, but with different temperature gradients (the white line), defined according to the prescribed Moho temperature. Extension velocity of 1.5 cm/yr is prescribed on both left and right boundaries. To ensure global mass conservation, new material is added to the model through the upper and lower boundary according to the prescribed vertical velocities (see text for details).

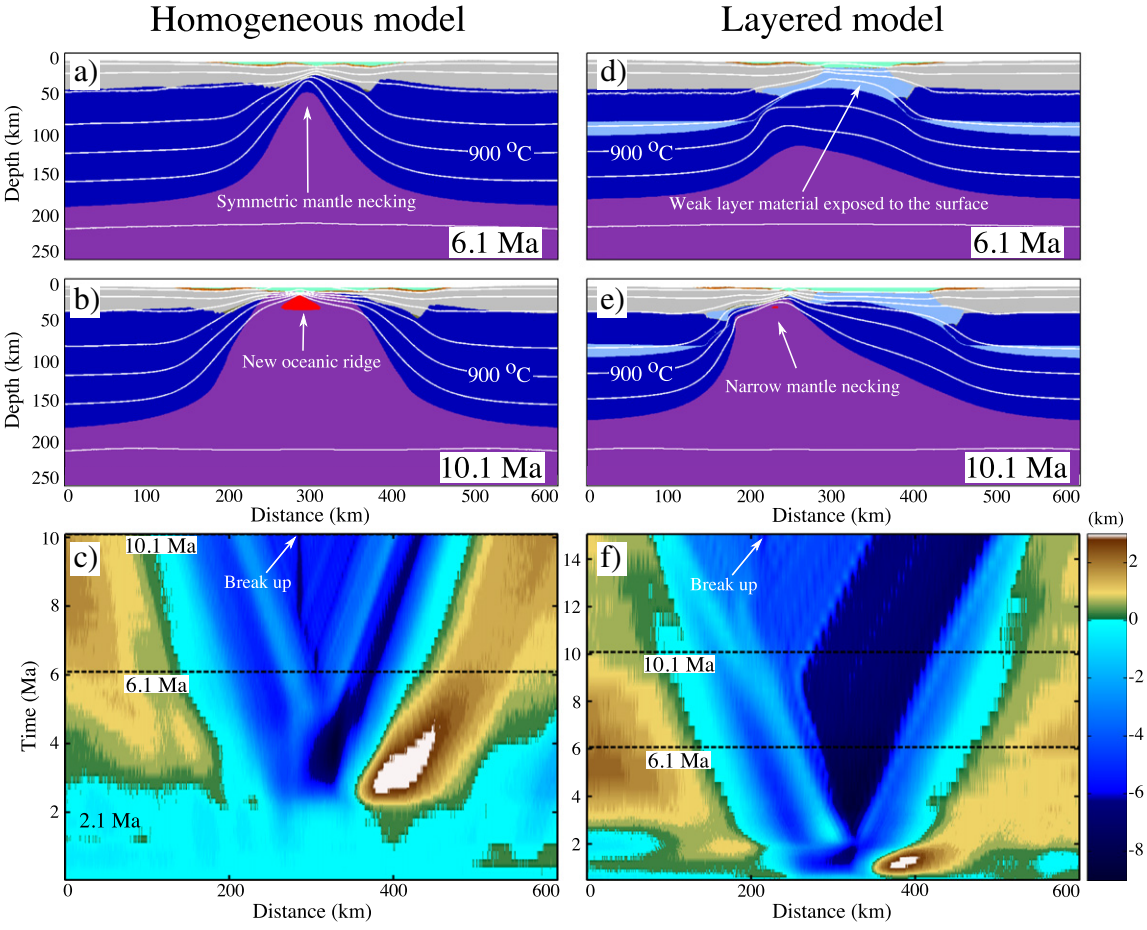

Fig. 3. Extension of the homogeneous and layered models shown by composition (a, b, d, and e) and topography (c, f). White lines in the composition snapshots are isotherms, with an interval of 200 °C. Depth (here and in the following the depth is given for the top surface of the weak layer) and thickness of the weak layer are 90 and 20 km, respectively. The initial Moho temperature is 450 °C. Shear heating is included, whereas plastic strain weakening is not employed.

dimensions in x and y directions; l_a is the thickness of the sticky air layer. v_{xl} and v_{yl} have minus signs which means that they are in the opposite directions with respect to v_{xr} and v_{yu} (x is positive rightward and y is positive downward), respectively.

With a weak sticky air layer overlain, the crustal surface is approximated as a free surface (Crameri et al., 2012) that can thus deform spontaneously. Our erosion/sedimentation model is highly simplified and uses gross-scale erosion/sedimentation rates which are independent

Fig. 4. Effect of the depth and thickness of the weak layer on lithospheric extension. The thickness of the weak layer varies from 10km (a–e) to 20km (f–j). The depth of the weak layer increases gradually from 60 to 180km. Dynamic evolution of the models is shown with thinning factor, which is the normalized lithospheric thinning: $(l_0-l)/l_0$, where l_0 is the original lithospheric thickness, l is the lithospheric thickness at a certain time. When thinning factors reach 1, lithospheric breakup occurs. One composition snapshot (zoomed in) is shown for each model. The red dashed line distinguished the narrow mantle necking (above) and the widespread mantle necking (below). The interval of temperature isotherm is 200°C.

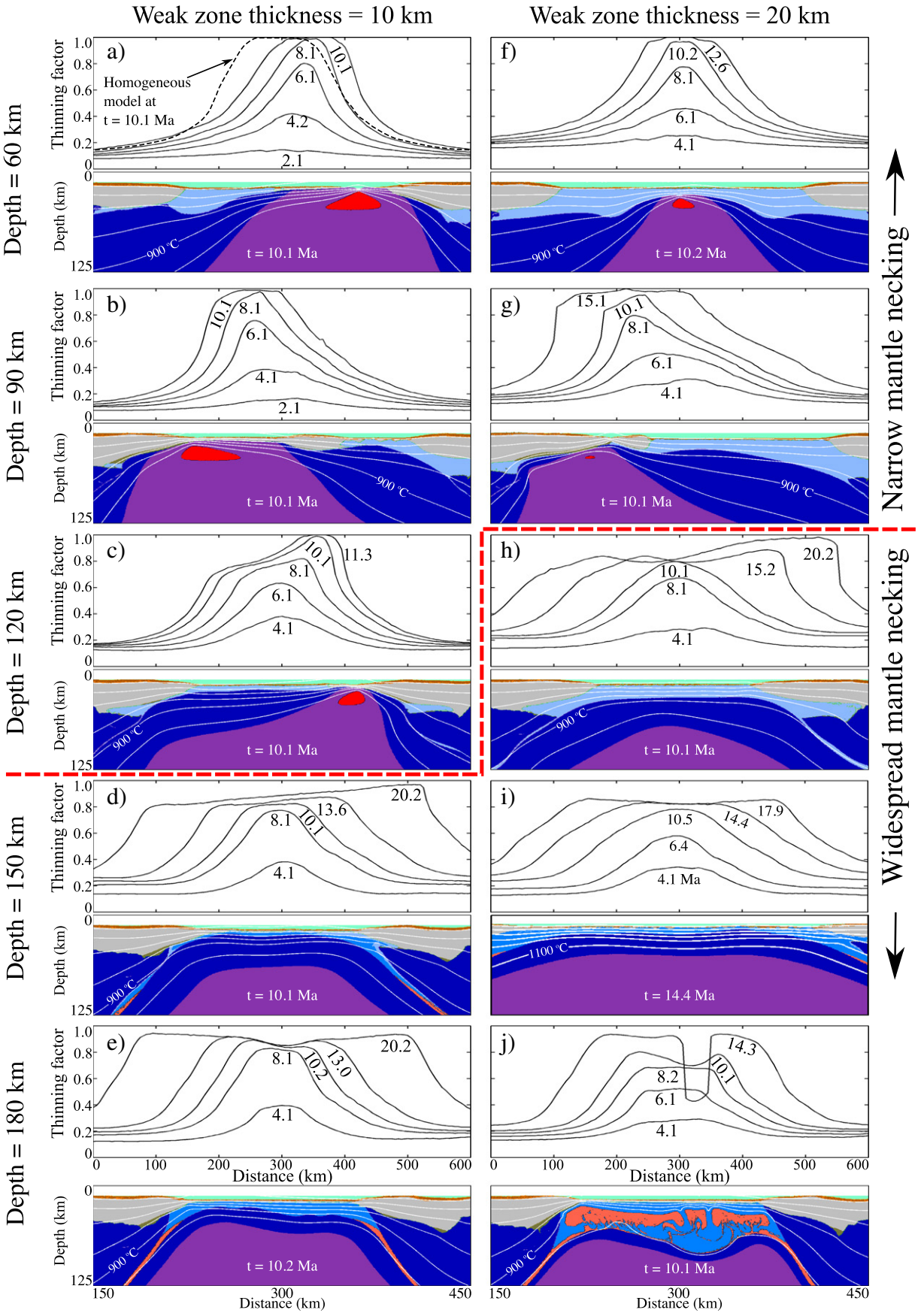
Weak zone thickness = 10 km
Weak zone thickness = 20 km
Depth = 60 km
Depth = 90 km
Depth = 120 km
Depth = 150 km
Depth = 180 km
Narrow mantle necking
Widespread mantle necking
Thinning factor
Depth (km)
Distance (km)
a)
b)
c)
d)
e)
f)
g)
h)
i)
j)
Homogeneous model at t = 10.1 Ma
900 °C
1100 °C
t = 10.1 Ma
t = 10.2 Ma
t = 14.4 Ma
4.1 Ma

of local elevation and topography slopes (Burov and Cloetingh, 1997). We use moderate erosion/sedimentation rate (0.315 mm/yr) which falls within naturally observed ranges. Erosion and sedimentation on the crustal surface are implemented by solving the transportation equation on the Eulerian nodes at each time step (Gerya and Yuen, 2003b):

$$\frac{\partial y_{es}}{\partial t} = v_y - v_x \frac{\partial y_{es}}{\partial x} - v_s + v_e \quad (14)$$

where y_{es} is the vertical position of the crustal surface; v_y and v_x are the vertical and horizontal velocity components on the crustal surface; v_s and v_e are the sedimentation and erosion rates, respectively, which correspond to the following relations: $v_s = 0$ and $v_e = 0.315$ mm/yr for $y_{es} < 10$ km, $v_s = 0.315$ mm/yr and $v_e = 0$ for $y_{es} \geq 10$ km (the initial depth of the crustal surface is 10 km).

3. Modeling results

3.1. Influence of lithospheric mantle stratification

Our numerical models generate typical rifting features (Braun and Beaumont, 1989; Zuber and Parmentier, 1986), such as the narrow mantle necking that develops following the narrow perturbation, the elevated geotherm caused by thermal convection and conduction, and the surface topography consisting of a major central depression and uplifted rift flanks (Fig. 3). As shown in a previous study (Liao et al., 2013), the layered model (including a weak layer within the mantle lithosphere) has distinct extension and breakup processes compared to that of the homogeneous model (without the weak layer). The weak layer enhances deformation of the overlying mantle and crust (crustal breakup occurs much earlier and weak material is exposed to the surface), but inhibits deformation of the underlying mantle and delays upwelling of the asthenosphere. This occurs because the accumulated weak material accommodates the space generated by extension. The weak layer also introduces lateral heterogeneity, which leads to asymmetric mantle necking (Fig. 3e). Since the deformation of the mantle lithosphere is inhibited, lithospheric breakup completes relatively late (Fig. 3e). Compared to the homogeneous model which generates relatively symmetric passive margins, layered model generates asymmetric margins (Fig. 3f). Sedimentation and erosion processes can significantly influence the rifting dynamics and surface topography (Buiter et al., 2009; Burov and Poliakov, 2001), however, the sedimentation/erosion is implemented in a highly simplified way in our models which only gives the first order features of the surface topography.

3.2. Depth and thickness of the weak layer

Initial depth and thickness of the weak layer influence lithospheric extension (Fig. 4). With a shallower weak layer, mantle melting due to decompression and the followed lithospheric breakup occur earlier. The thickness of the weak layer has a similar effect, i.e., a thinner weak layer promotes earlier decompression melting and continental breakup. In contrast, a deeper or thicker weak layer favors distributed lithospheric extension and widespread mantle necking/asthenosphere upwelling. If the weak layer locates sufficiently deep approaching the LAB, due to the high lithospheric temperature and the lowered solidus of the weak (hydrated) layer, partial melting is generated spontaneously with extension in the weak layer, which can change the dynamics of deformation. When the partially molten weak layer material reaches the crustal surface, it solidifies and becomes denser, and as a result, the exposed weak material drips into the asthenosphere due to the negative buoyancy (Fig. 4j). Here, we identify two deformation patterns: 1) narrow/localized and 2) widespread mantle necking (distinguished by a red dashed line in Fig. 4). The weak layer decouples the underlying lithospheric mantle (lower lithosphere—LL) from the overlying lithospheric mantle and crust (upper lithosphere—UL) (stress snapshots in Fig. 5). The major shear zones in the UL form along the weak layer channel and become widespread with extension (Fig. 5). A late strain localization (narrow mantle necking/asthenosphere upwelling area) forms in the LL after a certain extension since the uppermost part of the LL behaves brittlely (Fig. 5). The UL shear zones widen the rifting area while the late LL strain localization promotes narrow mantle necking/asthenosphere upwelling and continental breakup. Therefore model evolution is governed by the extension in the UL and LL. With a shallow weak layer, the strain localization in the LL occurs earlier and leads to a narrow mantle necking (Figs. 4c, 5a). In contrast, with a deep weak layer, strain localizes in the LL relatively late and the UL shear zones widen the rifting area greatly.

Asymmetric brittle extension is dominant in the early extension stage, followed by symmetric or asymmetric ductile-dominated deformation (Liao et al., 2013), generating the so-called asymmetric–symmetric (AS) or asymmetric–asymmetric (AA) deformation patterns proposed by Huismans and Beaumont (2002). In our study, most of the layered models produce an AA pattern, i.e. asymmetric brittle deformation followed by asymmetric ductile deformation (Fig. 4). Initial asymmetric perturbations are introduced by the randomly distributed markers in the model, and have been amplified by shear heating. As a consequence, one branch of the major conjugate shear zones that formed around the weak seed becomes dominant while another one is gradually abandoned. Since it is randomly chosen which of the two branches becomes dominant, both leftward and rightward asymmetric shear zones are generated in the brittle part of the lithosphere. Formation of the asymmetric pattern of mantle necking/asthenosphere upwelling is related with the strain localization in the lower lithosphere (LL) underneath the weak layer (Fig. 5). Asymmetric strain localization in the LL has a strong relation with the laterally accumulated weak layer material which distributes asymmetrically along the horizontal direction (Figs. 4h, 5b), since lithospheric lateral heterogeneity greatly affects strain localization (Le Pourhiet et al., 2004; Pascal and Cloetingh, 2002).

3.3. Effects of Moho temperature

The rheological structure (brittle–ductile layering) which defines the distribution of lithospheric strength, is to first order, a key factor controlling lithosphere deformation (Afonso and Ranalli, 2004; Burov and Watts, 2006). Most of the lithospheric strength is located in the upper brittle part of the crust and uppermost part of the lithospheric mantle (Brace and Kohlstedt, 1980; Kohlstedt et al., 1995). Therefore, lithosphere deformation can be dominated either by the upper crust or uppermost lithospheric mantle, depending on which accumulates the most stress (Behn et al., 2002; Gueydan et al., 2008). The Moho temperature plays a significant role on lithospheric strength distribution, as a high Moho temperature can dramatically reduce the strength of the uppermost lithospheric mantle. The work done by Gueydan et al. (2008) shows that Moho temperature affects the strength ratio between crust and mantle and leads to two end-member rifting patterns: low Moho temperature promotes the formation of narrow rifting while high Moho temperature favors wide rifting. With sufficiently high Moho temperature (where the heat can be inherited from previous collision), partial melting likely occurs in the lower crust, which leads to lower crustal dome (core complex model) and generates smooth Moho topography (Buck, 1991; Schenker et al., 2012).

In this section, the influence of higher Moho temperature on the lithospheric thermal–mechanical structures and lithospheric extension has been studied. Fig. 6 shows one-dimensional initial temperature distributions and stress envelops with respect to different initial Moho temperatures. The 1D calculation is based on the initial lithospheric structure (Fig. 2) and rock properties (Table 3) used in our 2D numerical modeling. The 1D lithospheric strength is calculated by taking the minimum value between the linear Mohr–Coulomb plastic yielding and the power-law dislocation creep under a constant strain rate. Higher Moho

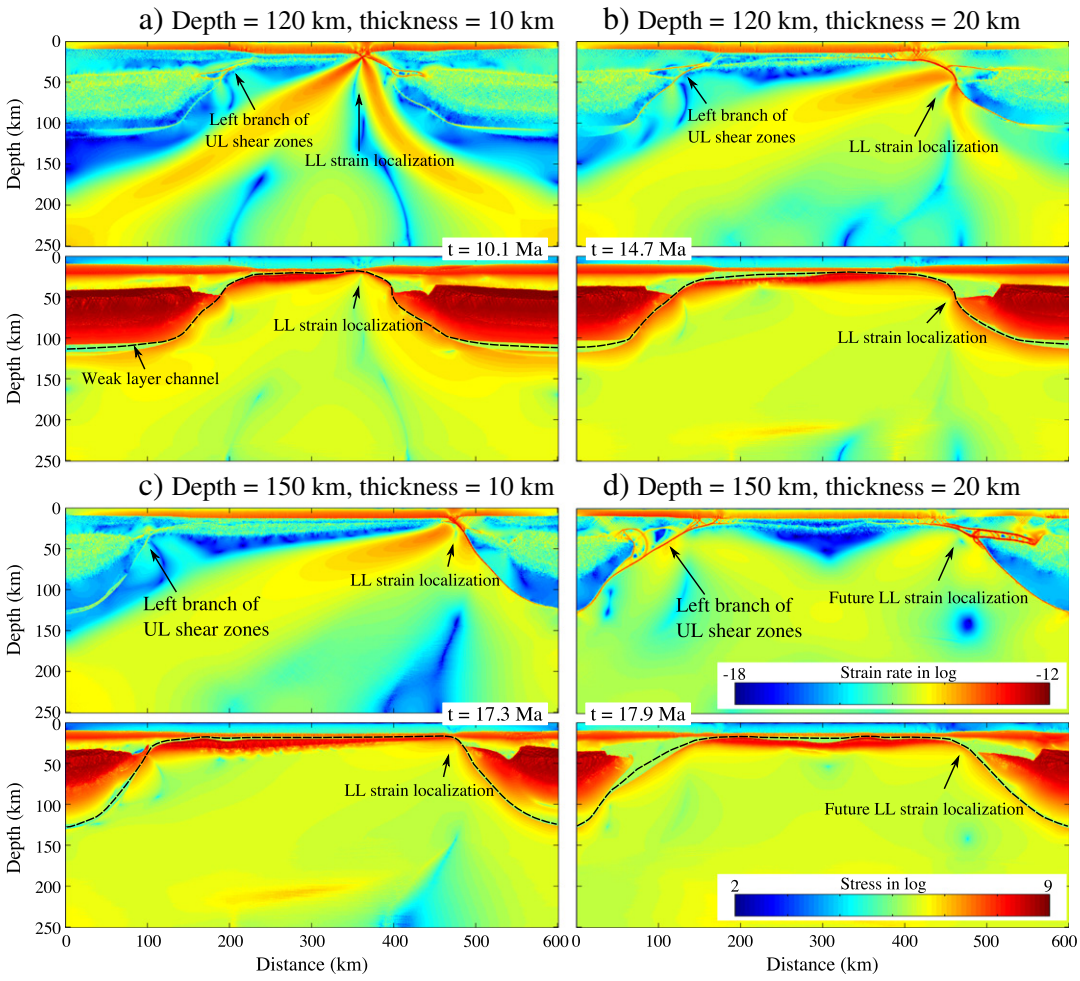

Fig. 5. Influence of the depth and thickness of the weak layer on strain localization in the upper lithosphere (UL) and lower lithosphere (LL) separated by the weak layer. The second invariant of strain rate is shown in the upper panel while the second invariant of deviatoric stress is shown in the lower panel. Note that a, b, c, and d corresponds to c, d, h, and i in Fig. 4, respectively.

temperatures indicate hotter lower crust as well as hotter uppermost lithospheric mantle. The strength peak of the uppermost mantle lithosphere decreases rapidly with increasing Moho temperature (Fig. 6b),

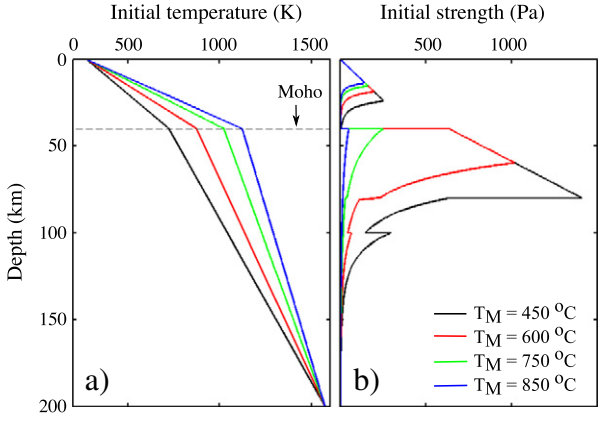

Fig. 6. 1D initial temperature distribution (a) and lithospheric strength (b) with respect to different Moho temperatures. The 1D lithospheric strength is computed by taking the minimum value between the linear Mohr–Coulomb yielding stress and the power-law dislocation creep stress under a constant strain rate (1.6×10^{-15} s^{-1}). Related parameters are listed in Table 3.

as high temperature reduces mantle viscosity exponentially. With Moho temperature higher than 750 °C, deformation in the upper mantle is entirely governed by dislocation creep. As a result, deformation does not localize into large plastic shear zones but remains broadly distributed, thus generating flat Moho topography.

In both the homogeneous and layered models, a higher Moho temperature leads to more distributed lithospheric extension in the early extension stage and strain localizes relatively late (Fig. 7a, b, d, and e). High Moho temperature inhibits the formation of lithospheric necking, as high geotherm deactivates brittle/plastic deformation (and the perturbation caused by the weak seed becomes subtle) which has been regarded as an important factor leading to necking (Bassi, 1991; Bassi et al., 1993). If the Moho temperature is higher than the threshold (~800 °C), extension dynamics significantly changes, as a partial molten layer is generated in the lower crust in the beginning of extension (Fig. 7c, f). Buoyant instabilities drive the deformation in the molten crustal layer, forming crustal domes. The location of the lower crustal domes is not defined by the initial weak seed, but is determined from the perturbations generated by Rayleigh–Taylor instability induced by lower crustal melting. Crustal convection cells will form in the molten lower crustal layer once the Rayleigh number of the molten lower crust is larger than the critical Rayleigh number (Schenker et al., 2012; Turcotte and Schubert, 2002). For the layered model, the influence of the high initial Moho temperature on lithospheric extension is similar to that in the homogeneous model. However, the weak layer enhances

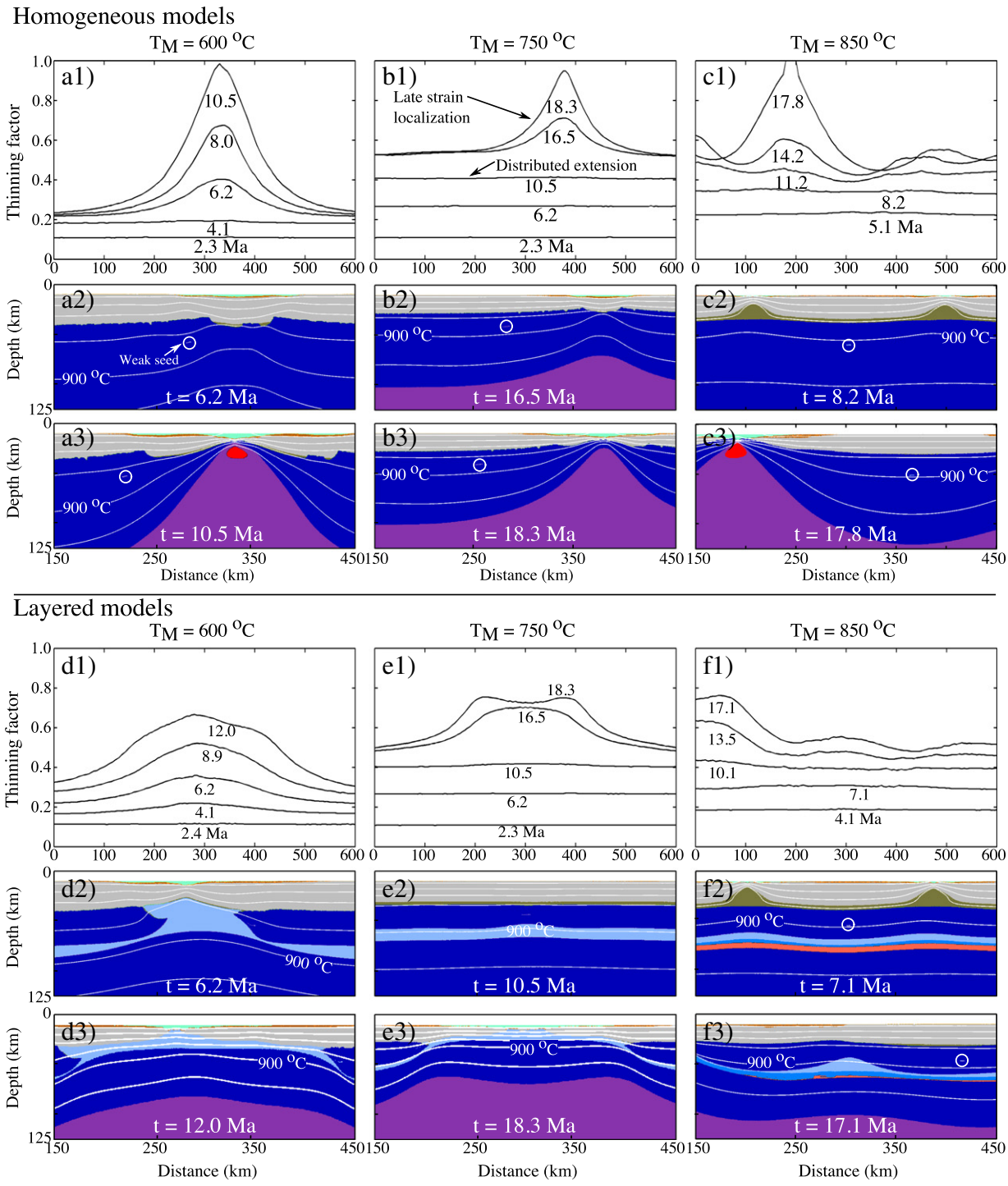

Fig. 7. Model evolution shown by thinning factors and composition snapshots for the homogeneous and layered models with respect to high initial Moho temperatures. Also see Fig. 3 for the homogeneous and layered models which have a Moho temperature of 450 °C. Note that high Moho temperatures promote widespread mantle necking (d3 and e3). Weak seed location is marked by the white circle in the models where strain localization avoids the weak seed. The interval of temperature isotherm is 200 °C.

the deformation of the overlying rock (since strain localizes on the weak seed) and promotes widespread mantle necking which leads to late lithospheric breakup (Fig. 7d1–d3, e1–e3).

3.4. Effects of shear heating and plastic strain weakening

Shear heating is an important heat generation process which is related to mechanical energy dissipation during irreversible deformation. 1D models show that shear heating could cause ductile strength decrease by a factor of 10 due to a temperature increase during crustal thickening under a realistic constant strain rate (Hartz and Podladchikov, 2008). 2D numerical modeling shows that shear heating is significant along localized deformation zones, where the heat generation by shear heating is higher than that by radiogenic heating in crust (Burg and Gerya, 2005). This could explain the observed high metamorphic temperatures in some orogenic areas, where thicker radiogenic crust is not sufficient to generate such high temperatures (Burg and Gerya, 2005) and thermal inversion (Duprat-Oualid et al., 2013).

Fig. 8 compares the temperature perturbation caused by shear heating during lithospheric extension in the homogeneous and layered

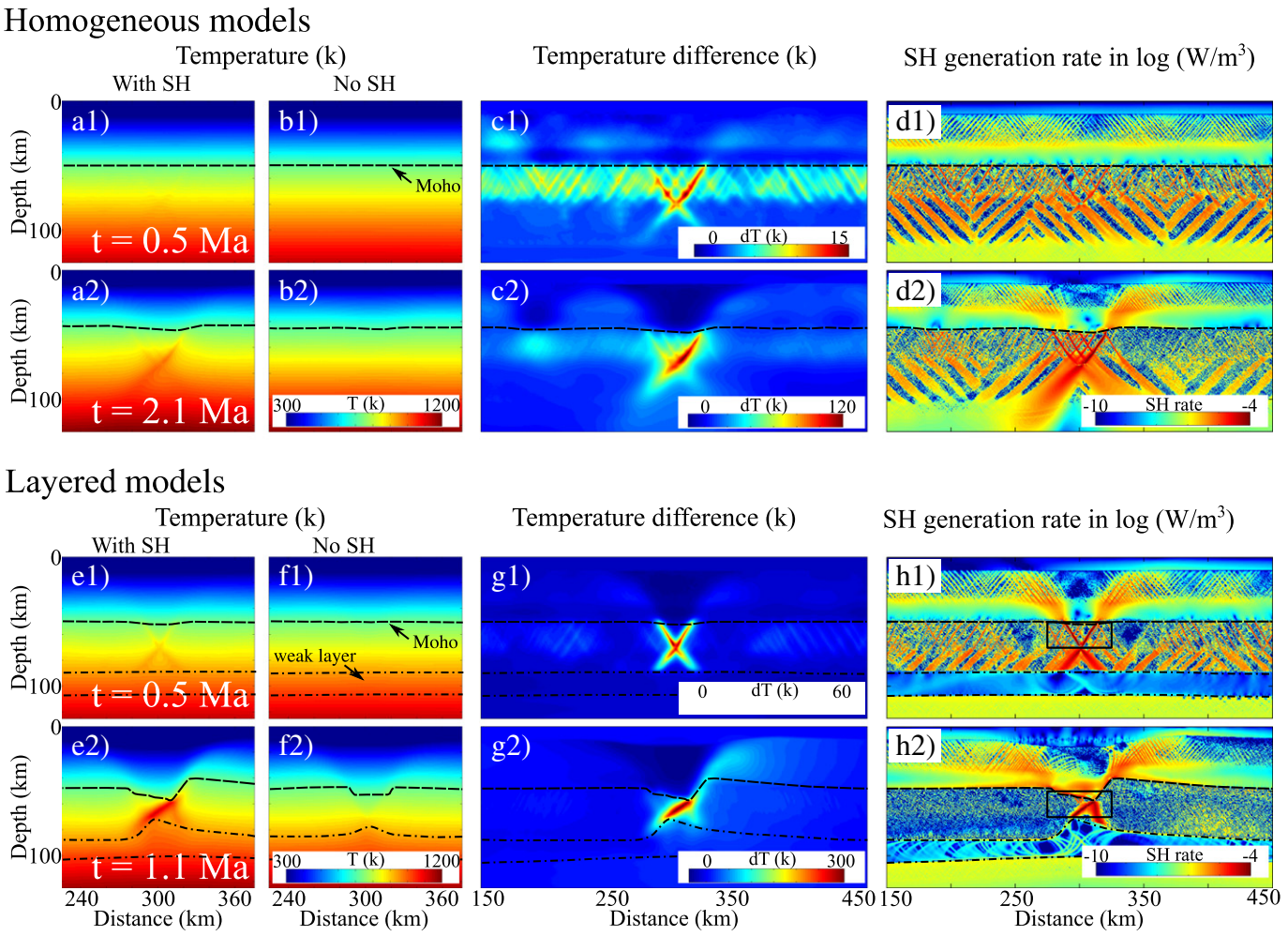

Fig. 8. Temperature perturbation caused by shear heating in the homogeneous and layered models. Along the major shear zones, shear heating (d1–d2, h1–h2) is 2 orders of magnitude larger than the radioactive heating (Table 3), which could cause large temperature difference (c1–c2, g1–g2) compared to the models without shear heating (b1–b2, f1–f2). SH—shear heating. The rectangles marked in h1 and h2 show the data area used in Fig. 9.

models. Shear heating generates significant temperature perturbations (Fig. 8a, c, e, and g) along the major shear zones locating around the initial weak seed. The temperature increase due to shear heating is in excess of 100 and 300 K along the major shear zones in the homogeneous and layered models, respectively. Symmetric temperature perturbations gradually become asymmetric as shear heating amplifies asymmetric perturbations along major shear zones. The shear heating along the major shear zones is two orders of magnitude lager than the crustal radioactive heating (1.75×10^{-6} W/m^3) (Turcotte and Schubert, 2002). Compared to the homogeneous model, the layered model has larger and faster temperature increase (Fig. 8g2), because the weak layer enhances localized deformation in the upper lithosphere in the early extension stage. Shear heating has a strong dependence on stress during brittle deformation (Fig. 9). Before 0.67 Ma, shear heating is proportional to the increasing strain rate (since stress level remains relatively constant during this initial stage, cf. Fig. 9a, c, and d), but has an inverse relationship with the effective viscosity (Fig. 9b). In contrast, after 0.67 Ma, shear heating decreases proportional to the decreasing stress (Fig. 9a, d).

A purely phenomenological plastic strain weakening (by reducing the plastic yielding stress after a certain strain) is commonly used in the numerical modeling models on continental rifting and oceanic spreading (Gerya, 2013) (and reference therein). Plastic strain weakening does not reflect direct physical processes, but it may represent various weakening effects, in particular, weakening due to the presence of fluids along fault zones (Gerya, 2013). Plastic strain weakening promotes asymmetric extension (Huismans and Beaumont, 2002). The onset of strain weakening, the magnitude of reduction in strength, and the rate of weakening can influence the lithospheric deformation (Allken et al., 2011; Frederiksen and Braun, 2001). In this study, we implement strain weakening by linearly reducing the coefficient of internal friction (to one-half of the initial values) when plastic strain is between 0.25 and 1.25. The effects of plastic strain weakening and shear heating are compared in Fig. 10. Both shear heating and strain weakening enhance deformation in the brittle part of the lithosphere (Fig. 10b1, c1), and combination of these two effects therefore has a more significant influence on enhancing the lithospheric extension (Fig. 10d1–d2). In the layered model, shear heating and strain weakening play a significant role on generating asymmetric extension (Fig. 10f2, g2, and h2). Shear heating and plastic strain weakening effects are further compared in terms of boundary force in Section 5.2.

4. Discussion

4.1. Comparison with natural examples

The North China craton (NCC) provides an example of craton destruction, although the active mechanisms triggering deformation are still not clear (Menzies et al., 2007). The western block of the NCC is relatively stable, whereas the eastern block underwent significant

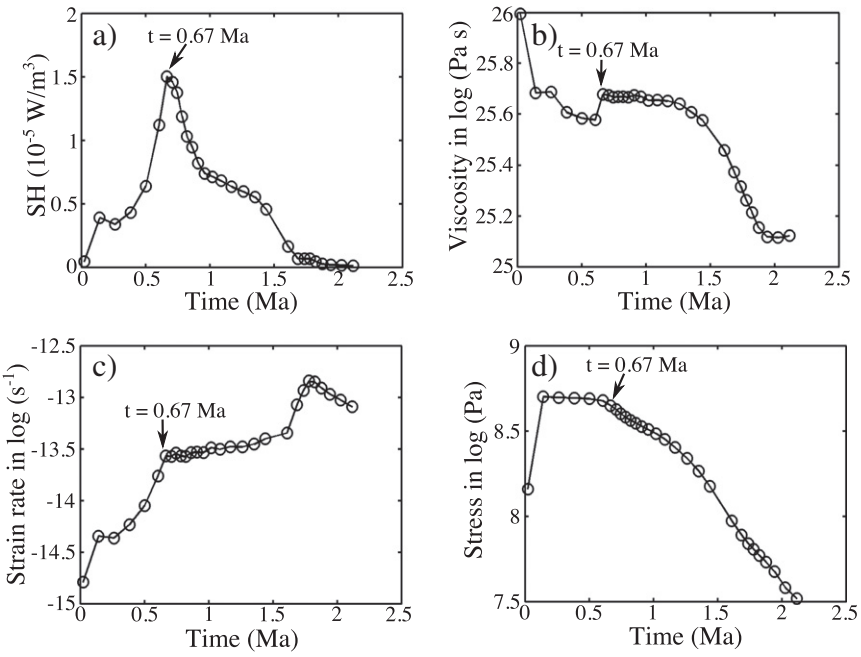

Fig. 9. Evolution of (a) mean shear heating (SH), (b) mean effective viscosity, (c) mean second invariant of strain rate and (d) mean second invariant of deviatoric stress. These mean values are averaged in the area marked by the rectangles in Fig. 8.

destruction (Fig. 11a). Depleted Precambrian lithospheric mantle has been replaced by Mesozoic–Cenozoic fertilized mantle (Menzies et al., 2007). The present-day thickness of the eastern block is ~80 km (Fig. 11b), and the extension pattern is wide rifting (Fig. 11c), similar to the Basin and Range province (Lu et al., 2012; Menzies et al., 2007). Unlike the greatly curved lithosphere–asthenosphere boundary (LAB), the Moho boundary is flat (Fig. 11b). The duration of lithospheric thinning of the east block is over 100 Ma based on the magmatic events (Xu et al., 2009), suggesting slow extension of NCC. Re-hydration of lithospheric mantle may have occurred in the NCC (Lee et al., 2011) due to the Paleo-Pacific plate subduction (Zhao and Xue, 2010). Metasomatism is abundant in the NCC (Xu et al., 2008), and a metasomatized layer in

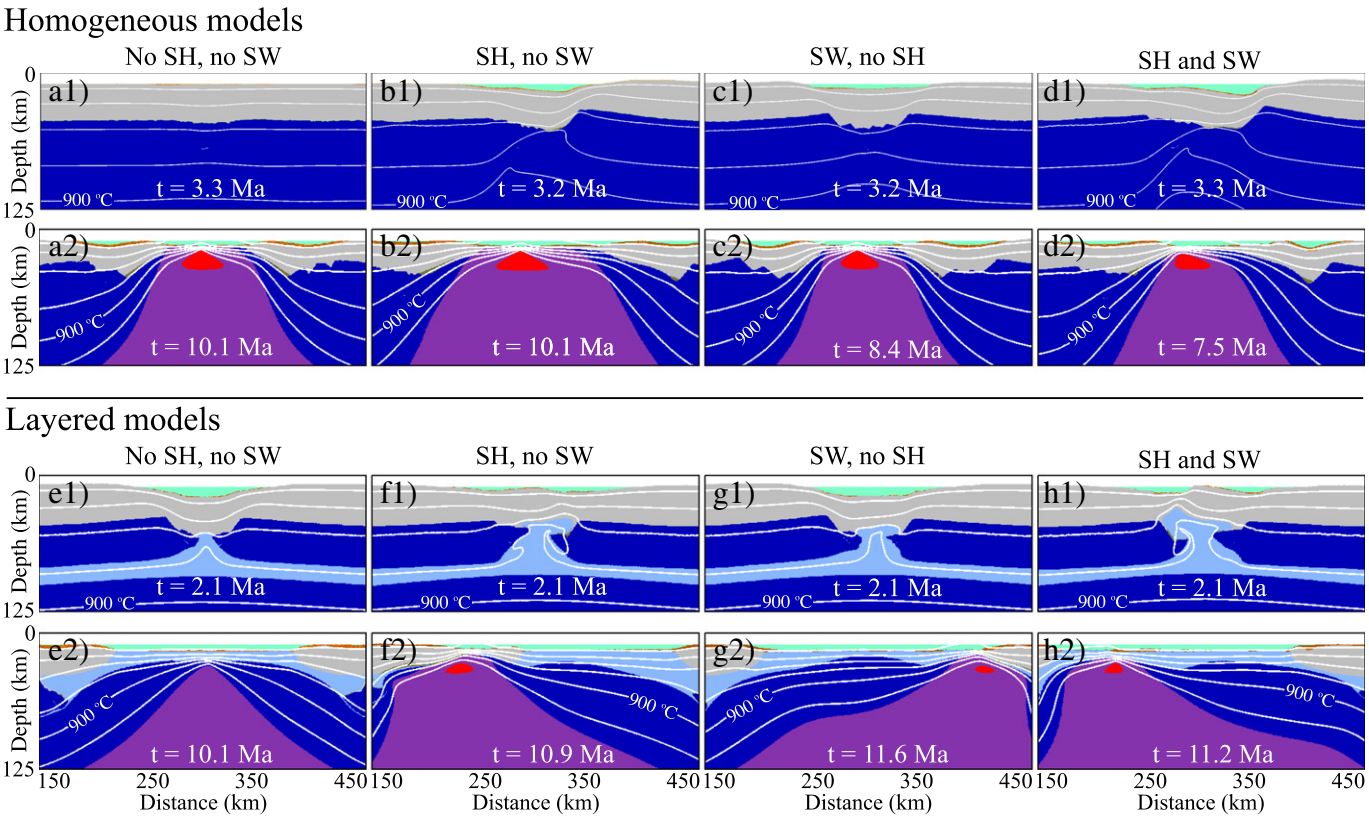

Fig. 10. Comparison between shear heating and strain weakening shown by the composition snapshots. SH—shear heating, SW—strain weakening. The interval of temperature isotherm is 200 °C.

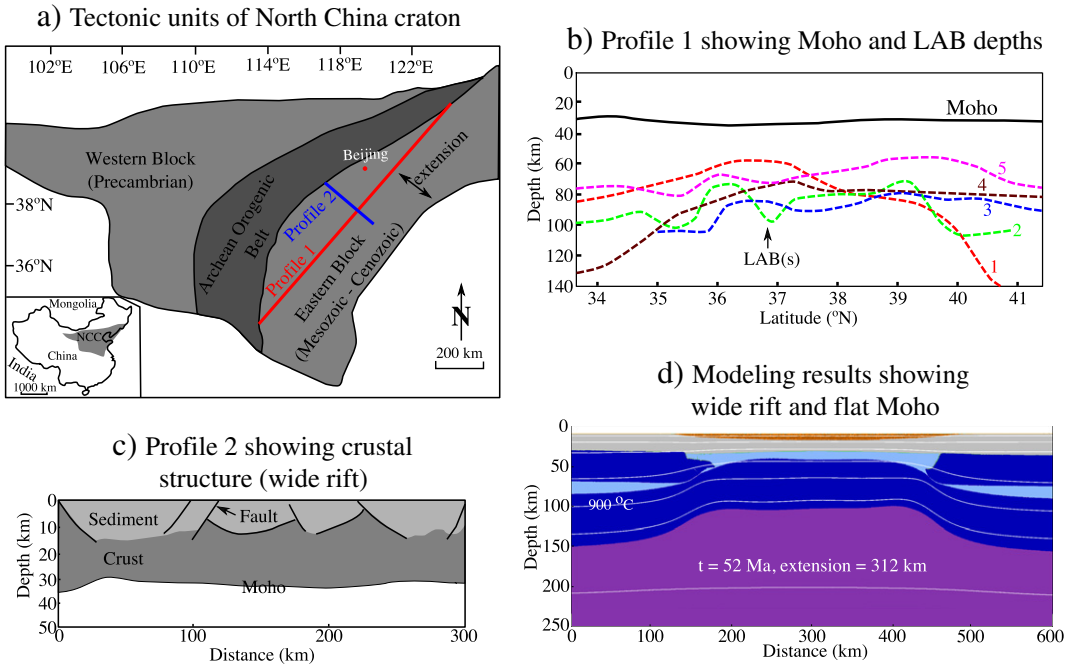

Fig. 11. Comparison with the North China craton (NCC). (a) Simplified tectonic unites of the NCC (modified after Polat et al., 2005). The east block of the NCC is in extensional regime (Kusky et al., 2007). (b) Lithospheric structure along profile 1. Dashed color lines indicate the lithosphere–asthenosphere boundary (LAB) based on different methods (modified after Zhang et al., 2012). 1—gravity inversion, 2—geotherm inversion, 3—receiver function imaging, 4—surface wave tomography, 5—MT. (c) Crustal structure along profile 2 showing wide rift structure (modified after He et al., 2009). (d) Modeling results with slow extension rate (half rate 0.3 cm/yr) showing wide rift development. Initial Moho temperature is 450 °C.

the lithospheric mantle is proposed by Xu (2001). Our layered model (where the weak layer represents metasomatized/hydrated composition) with a slow extension rate (half rate 0.3 cm/yr) generates wide rift with a flat Moho topography (Fig. 11d). Due to slow and long-time extension, the rift basin is fulfilled with thick sediment. Furthermore, the boundary force required to keep the constant extension rate of the layered model

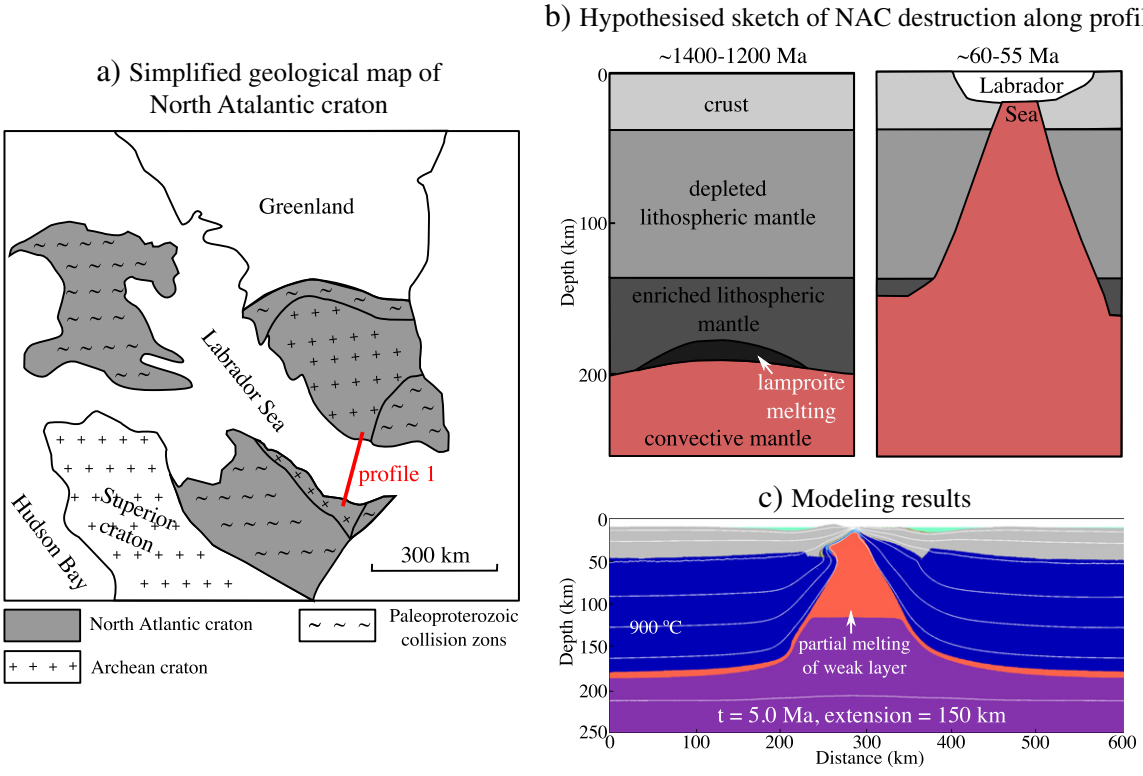

Fig. 12. Comparison with the North Atlantic craton (NAC). (a) Simplified geological map of the NAC (modified after Tappe et al., 2007). (b) Hypothesized sketch of NAC destruction through chemical erosion (modified after Tappe et al., 2007). (c) Modeling results with a weak layer locating at the base of the lithosphere. Half extension rate is 1.5 cm/yr, and Moho temperature is 450 °C.

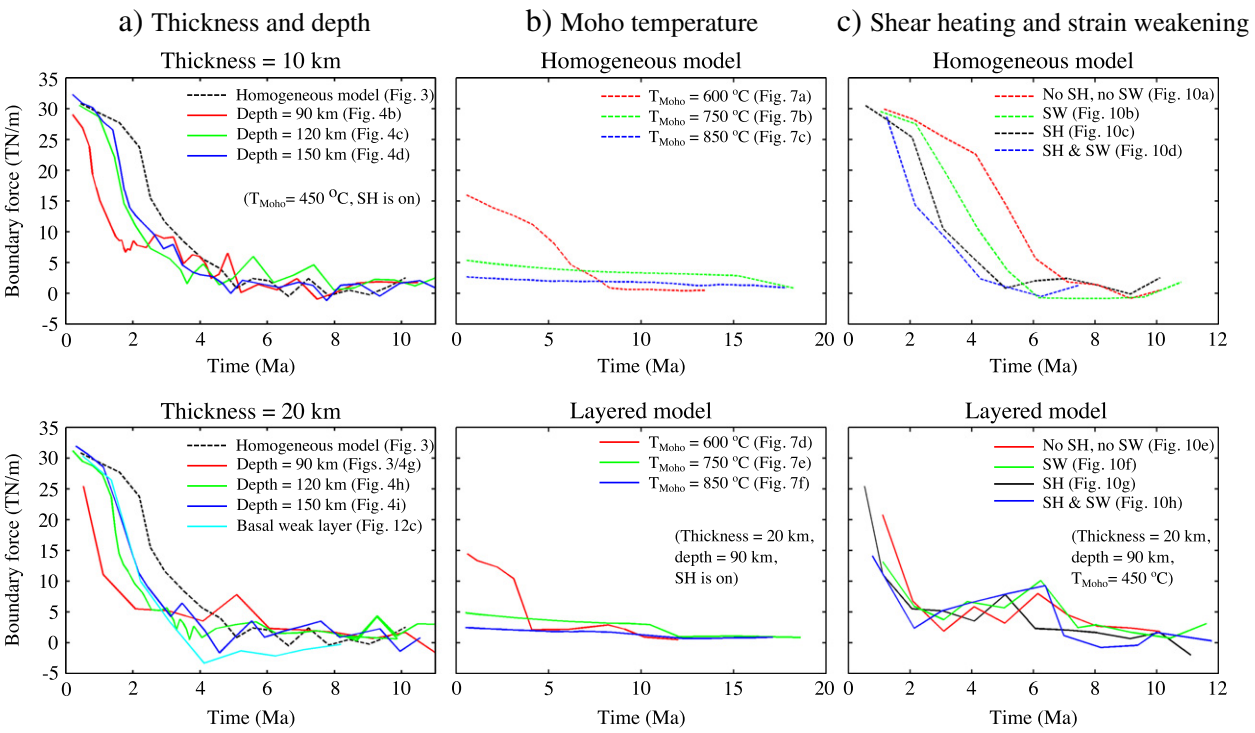

Fig. 13. Boundary force evolution for different models. T_M—Moho temperature. SH—shear heating, SW—strain weakening.

is much lower than that of the homogenous model, indicating that the layered model is relatively easier to undergo deformation (Liao et al., 2013).

The North Atlantic craton (NAC) also has experienced dramatic destruction (Fig. 12), where the continent broke up and Labrador Sea formed at ~60 Ma (Tappe et al., 2007). Based on a geochemical study, a chemical erosion hypothesis is proposed by Tappe et al. (2007). The lower part of the NAC lithosphere has been enriched during the long-term craton evolution. Lamproite melting occurs and accumulates at the base of the lithosphere, which greatly aids lithospheric thinning during Mesozoic continental extension. Lithospheric deformation with influence of basal melts is simulated with our numerical model, which includes a weak layer (representing accumulated melts) seating at the base of the lithosphere (Fig. 12c). Due to the high lithospheric temperature and the lowered solidus of the weak layer, partial melting generates in the weak layer spontaneously with extension, which enhances lithospheric deformation. Continental breakup completes much earlier (Fig. 12). The calculated boundary force becomes negative at ~4 Ma (Fig. 13a), indicating that the rapid upwelling of weak layer (with melting) drives lithosphere deformation and compressional force is even required to maintain the constant boundary extension rate. Therefore, basal melts indeed aids continental extension and breakup.

4.2. Boundary force

Boundary force is calculated (by integrating the normal stress along each side boundary, and taking the mean value between the left and right boundary forces) to evaluate the overall resistance of cratonic lithosphere to extension (Fig. 13). The layered model requires much lower boundary force in the early extension stage (<~5 Ma), because the buoyant weak layer material enhances deformation of the overlying mantle and crust. This indicates that the layered model is easier to initiate and undergo deformation in the early extension stage under the same stress regime induced by mantle convection and/or slab pull. Boundary force drops rapidly in both the layered and homogeneous models in the early stage, due to the formation of the large shear zones in the brittle part of the lithosphere. The influence of the thickness of the weak layer on boundary force is not significant, but the depth of the weak layer dramatically affects boundary force, as the shallower weak layer decreases the strength of the lithosphere more significantly (Fig. 13a). Moho temperature reduces the strength of the lithosphere greatly, as a consequence, boundary forces have smaller magnitudes and smooth variations (Fig. 13b). Shear heating and strain weakening both can decrease the boundary force, however models with the weak layer show stronger variability than the homogeneous models (Fig. 13c).

As discussed in a previous study (Liao et al., 2013), the presence of the weak layer enhances cratonic extension, but may not be sufficient alone to initiate deformation in the first place. Availability of the extension force in the beginning of extension is the most critical condition to initiate deformation, whereas presence of the weak layer does not seem to be capable of notably reducing this initially required force. Therefore the global presence of the weak layer does not conflict with the observations that most cratons still maintain stability in the present day. Evolution of the North China craton is strongly affected by complex and dynamic tectonics, such as continental collision (Menzies et al., 2007; Zheng et al., 2009) and Paleo-Pacific subduction (Zhao and Xue, 2010). The lithosphere of the NCC may have been largely modified and weakened before the intense extension that may had been assisted by the weak layer. The North Atlantic craton experienced long-time weak deformation (chemical erosion) from Precambrian to Mesozoic which sufficiently weakened the lithosphere, and after that the accumulated basal melts triggered and enhanced the intensive lithospheric thinning/breakup in the late Mesozoic (Tappe et al., 2007). Therefore, extra mechanisms (for instance the elevated geotherm (Fig. 13b) due to plume-induced magmatism) are needed to trigger an intense cratonic deformation and breakup.

5. Conclusion

Our results show that a mid-lithospheric weak layer changes the dynamics of cratonic extension. The weak layer has a twofold effect: it enhances deformation of the overlying mantle and crust, and inhibits deformation of the underlying mantle. The weak layer decouples the

overlying lithospheric mantle and crust from the underlying mantle, and its depth influences lithospheric extension. Two extension patterns have been identified: 1) narrow and localized mantle necking is favored by a shallow and thin weak layer, as well as low Moho temperature, and 2) widespread mantle necking which leads to wide rifting is promoted by a deep and thick weak layer, as well as high Moho temperatures. Shear heating and plastic strain weakening promotes asymmetric extension, and this effect can be enhanced by the presence of a weak mantle layer. The presence of a weak lithospheric mantle layer may not be sufficient to initiate an intense cratonic deformation and break-up, but this weak layer can indeed enhance deformation/thinning process by lowering the required extensional boundary force.

References

Abt, D.L., Fischer, K.M., French, S.W., Ford, H.A., 2010. North American lithospheric discontinuity structure imaged by ps and sp receiver functions. J. Geophys. Res. 115, 1–24. http://dx.doi.org/10.1029/2009JB006914.

Afonso, J.C., Ranalli, G., 2004. Crustal and mantle strengths in continental lithosphere: is the jelly sandwich model obsolete? Tectonophysics 394, 221–232. http://dx.doi.org/10.1016/j.tecto.2004.08.006.

Allken, V., Huismans, R.S., Thieulot, C., 2011. Three-dimensional numerical modeling of upper crustal extensional systems. J. Geophys. Res. 116, 1–15. http://dx.doi.org/10.1029/2011JB008319.

Bassi, G., 1991. Factors controlling the style of continental rifting: insights from numerical modeling. Earth Planet. Sci. Lett. 105, 430–452.

Bassi, G., Keen, C.E., Potter, P., 1993. Contrasting styles of rifting: models and examples from the eastern canadian margin. Tectonics 12, 639–655.

Behn, M.D., Lin, J., Zuber, M.T., 2002. A continuum mechanics model for normal faulting using a strain-rate softening rheology: implications for thermal and rheological controls on continental and oceanic rifting. Earth Planet. Sci. Lett. 202, 725–740.

Bittner, D., Schmeling, H., 1995. Numerical modeling of melting processes and induced diapirism in the lower crust. Geophys. J. Int. 123, 59–70.

Brace, W.F., Kohlstedt, D.L., 1980. Limits on lithospheric stress imposed by laboratory experiments. J. Geophys. Res. 85, 6248–6252.

Braun, J., Beaumont, C., 1989. A physical explanation of the relation between flank uplifts and the breakup unconformity at rifted continental margins. Geology 17, 760–764.

Buck, W.R., 1991. Models of continental lithospheric extension. J. Geophys. Res. 96, 20161–20178.

Buiter, S.J.H., Pfiffner, O.A., Beaumont, C., 2009. Inversion of extensional sedimentary basins: a numerical evaluation of the localisation of shortening. Earth Planet. Sci. Lett. 288, 492–504. http://dx.doi.org/10.1016/j.epsl.2009.10.011.

Burg, J.P., Gerya, T., 2005. The role of viscous heating in barrovian metamorphism of collisional orogens: thermomechanical models and application to the lepontine dome in the central alps. J. Metamorph. Geol. 23, 75–95. http://dx.doi.org/10.1111/j.1525-1314.2005.00563.x.

Burov, E., Cloetingh, S., 1997. ?erosion and rift dynamics: new thermomechanical aspects of post-rift evolution of extensional basins? Earth Planet. Sci. Lett. 150, 7–26.

Burov, E., Poliakov, A., 2001. Erosion and rheology controls on synrift and postrift evolution: verifying old and new ideas using a fully coupled numerical model. J. Geophys. Res. 106, 16461–16481.

Burov, E.B., Watts, A.B., 2006. The Long-term Strength of Continental Lithosphere: "Jelly Sandwich" or "Crème Brûlée"? GSA Today 16.

Cammarano, F., Romanowicz, B., 2007. Insights into the nature of the transition zone from physically constrained inversion of long-period seismic data. Proc. Natl. Acad. Sci. 104, 9139–9144.

Carlson, R.W., Pearson, D.G., James, D.E., 2005. Physical, chemical, and chronological characteristics of continental mantle. Rev. Geophys. 43. http://dx.doi.org/10.1029/2004RG000156.

Chemenda, A., Deverchere, J., E. C., 2002. Three-dimensional laboratory modelling of rifting: application to the baikal rift, russia. Tectonophysics 356, 253–273.

Clauser, C., Huenges, E., 1995. Thermal conductivity of rocks, minerals. In: Ahrens, T.J. (Ed.), Rock Physics and Phase Relations. American Geophysical Union, Washington, DC, pp. 105–126.

Cooper, C.M., Lenardic, A., Levander, A., Moresi, L., 2006. Creation and preservation of cratonic lithosphere: Seismic constraints and geodynamic models. In: Benn, K., Mareschal, J.C., Condie, K.C. (Eds.), Archean Geodynamics and Environments, American Geophysical Union, Geophysical Monograph Series, pp. 75–88.

Crameri, F., Schmeling, H., Golabek, G.J., Duretz, T., Orendt, R., Buiter, S.J.H., May, D.A., Kaus, B.J.P., Gerya, T.V., Tackley, P.J., 2012. A comparison of numerical surface topography calculations in geodynamic modelling: an evaluation of the 'sticky air' method. Geophys. J. Int. 189, 38–54. http://dx.doi.org/10.1111/j.1365-246X.2012.05388.x.

Dunbar, J.A., Sawyer, D.S., 1988. Continental rifting at pre-existing lithospheric weakness. Nature 333, 450–452.

Duprat-Oualid, S., Yamato, P., Pitra, P., 2013. Major role of shear heating in intracontinental inverted metamorphism: inference from a thermo-kinematic parametric study. Tectonophysics 608, 812–831. http://dx.doi.org/10.1016/j.tecto.2013.07.037.

Frederiksen, S., Braun, J., 2001. Numerical modelling of strain localisation during extension of the continental lithosphere. Earth Planet. Sci. Lett. 188, 241–251.

Gerya, T., 2010. Introduction to Numerical Geodynamic Modelling. Cambridge University Press, UK.

Gerya, T.V., 2013. Three-dimensional thermomechanical modeling of oceanic spreading initiation and evolution. Phys. Earth Planet. Inter. 214, 35–52. http://dx.doi.org/10.1016/j.pepi.2012.10.007.

Gerya, T.V., 2014. Precambrian geodynamics: concepts and models. Gondwana Res. 25, 442–463. http://dx.doi.org/10.1016/j.gr.2012.11.008.

Gerya, T.V., Yuen, D.A., 2003a. Characteristics-based marker-in-cell method with conservative finite-differences schemes for modeling geological flows with strongly variable transport properties. Phys. Earth Planet. Inter. 140, 293–318. http://dx.doi.org/10.1016/j.pepi.2003.09.006.

Gerya, T.V., Yuen, D.A., 2003b. Rayleigh–Taylor instabilities from hydration and melting propel 'cold plumes' at subduction zones. Earth Planet. Sci. Lett. 212, 47–62. http://dx.doi.org/10.1016/S0012-821X(03)00265-6.

Gerya, T.V., Yuen, D.A., 2007. Robust characteristics method for modelling multiphase visco-elasto-plastic thermo-mechanical problems. Phys. Earth Planet. Inter. 163, 83–105. http://dx.doi.org/10.1016/j.pepi.2007.04.015.

Gray, R., Pysklywec, R.N., 2010. Geodynamic models of archean continental collision and the formation of mantle lithosphere keels. Geophys. Res. Lett. 37, 1–5. http://dx.doi.org/10.1029/2010GL043965.

Griffin, W.L., O'Reilly, S.Y., Natapov, L.M., Ryan, C.G., 2003. The evolution of lithospheric mantle beneath the kalahari craton and its margins. Lithos 71, 215–241. http://dx.doi.org/10.1016/j.lithos.2003.07.006.

Griffin, W.L., O'Reilly, S.Y., Doyle, B.J., Pearson, N.J., 2004. Lithosphere mapping beneath the North American Plate. Lithos 77, 873–922. http://dx.doi.org/10.1016/j.lithos.2004.03.034.

Griffin, W.L., O'Reilly, S.Y., Afonso, J.C., Begg, G.C., 2009. The composition and evolution of lithospheric mantle: a re-evaluation and its tectonic implications. J. Petrol. 50, 1185–1204. http://dx.doi.org/10.1093/petrology/egn033.

Gueydan, F., Morency, C., Brun, J.P., 2008. Continental rifting as a function of lithosphere mantle strength. Tectonophysics 460, 83–93. http://dx.doi.org/10.1016/j.tecto.2008.08.012.

Gung, Y., Panning, M., Romanowicz, B., 2003. Global anisotropy and the tickness of continets. Nature 422, 707. http://dx.doi.org/10.1038/nature01559.

Hartz, E.H., Podladchikov, Y.Y., 2008. Toasting the jelly sandwich: the effect of shear heating on lithospheric geotherms and strength. Geology 36, 331–334. http://dx.doi.org/10.1130/G24424A.1.

He, L., Hu, S., Yang, W., Wang, J., 2009. Radiogenic heat production in the lithosphere of sulu ultrahigh-pressure metamorphic belt. Earth Planet. Sci. Lett. 277, 525–538. http://dx.doi.org/10.1016/j.epsl.2008.11.022.

Hess, P.C., 1989. Origin of Igneous Rocks. Harward University Press, London, UK.

Hirschmann, M.M., 2000. Mantle solidus: experimental constraints and the effects of peridotite composition. Geochem. Geophys. Geosyst. 1. http://dx.doi.org/10.1029/2000GC000070.

Huismans, R.S., Beaumont, C., 2002. Asymmetric lithospheric extension: the role of frictional plastic strain softening inferred from numerical experiments. Geology 30, 211–214.

Huismans, R., Beaumont, C., 2011. Depth-dependent extension, two-stage breakup and cratonic underplating at rifted margins. Nature 473, 74–79. http://dx.doi.org/10.1038/nature09988.

Johannes, W., 1985. The significance of experimental studies for the formation of migmatites. In: Ashworth, J. (Ed.), Migmatites. Blackie, Glasgow, UK, pp. 36–85.

Karato, S., Jung, H., 1998. Water, partial melting and the origin of the seismic low velocity and high attenuation zone in the upper mantle. Earth Planet. Sci. Lett. 157, 193–207.

Katayama, I., Karato, S., 2008. Low-temperature, high-stress deformation of olivine under water-saturated conditions. Phys. Earth Planet. Inter. 168, 125–133. http://dx.doi.org/10.1016/j.pepi.2008.05.019.

Kohlstedt, D.L., Evans, B., Mackwell, S.J., 1995. Strength of the lithosphere: constraints imposed by laboratory experiments. J. Geophys. Res. 100, 17587–17602.

Kopylova, G.K., Russell, J.K., 2000. Chemical stratification of cratonic lithosphere: constraints from the northern slave craton, canada. Earth Planet. Sci. Lett. 181, 71–87.

Kusky, T.M., Windley, B.F., Zhai, M.G., 2007. Tectonic evolution of the north china block: from orogen to craton to orogen. Special Publications, 280. Geological Society, London, pp. 1–34. http://dx.doi.org/10.1144/SP280.1.

Le Pourhiet, L., Burov, E., Moretti, I., 2004. Rifting through a stack of inhomogeneous thrusts (the dipping pie concept). Tectonics 23. http://dx.doi.org/10.1029/2003TC001584.

Lee, C.T.A., Luffi, P., Chin, E.J., 2011. Building and destroying continental mantle. Annu. Rev. Earth Planet. Sci. 39, 59–90. http://dx.doi.org/10.1146/annurev-earth-040610-133505.

Lenardic, A., Moresi, L.N., 1999. Some thoughts on the stability of cratonic lithosphere: effects of buoyancy and viscosity. J. Geophys. Res. 104, 12747–12758.

Lenardic, A., Moresi, L., Muhlhaus, H., 2000. The role of mobile belts for the longevity of deep cratonic lithosphere: the crumple zone model. Geophys. Res. Lett. 27, 1235–1238.

Lenardic, A., Moresi, L.N., Muhlhaus, H., 2003. Longevity and stability of cratonic lithosphere: insights from numerical simulations of coupled mantle convection and continental tectonics. J. Geophys. Res. 108. http://dx.doi.org/10.1029/2002JB001859.

Liao, J., Gerya, T., Wang, Q., 2013. Layered structure of the lithospheric mantle changes dynamics of craton extension. Geophys. Res. Lett. 40, 1–6. http://dx.doi.org/10.1002/2013GL058081.

Lu, G., Kaus, B., Zhao, L., 2012. Thermal localization as a potential mechanism to rift cratons. Phys. Earth Planet. Inter. 186, 125–137. http://dx.doi.org/10.1016/j.pepi.2011.04.006.

Menzies, M., Xu, Y.G., Zhang, H.F., Fan, W.M., 2007. Integration of geology, geophysics and geochemistry: a key to understanding the north china craton. Lithos 96, 1–21. http://dx.doi.org/10.1016/j.lithos.2006.09.008.

Mercier, J.P., Bostock, M.G., Audet, P., Gaherty, J.B., Garnero, E.J., 2008. The teleseismic signature of fossil subduction: Northwestern Canada. J. Geophys. Res. 113. http://dx.doi.org/10.1029/2007JB005127.

Nettles, M., Dziewonski, A.M., 2007. Radially anisotropic shear velocity structure of the upper mantle globally and beneath North America. J. Geophys. Res. 113, 1–27. http://dx.doi.org/10.1029/2006JB004819.
O'Neill, C.J., Lenardic, A., Griffin, W.L., 2008. Dynamics of cratons in an evolving mantle. Lithos 102, 12–24. http://dx.doi.org/10.1016/j.lithos.2007.04.006.
O'Neill, C.J., Kobussen, A., Lenardic, A., 2010. The mechanics of continental lithosphere–asthenosphere coupling. Lithos 120, 55–62. http://dx.doi.org/10.1016/j.lithos.2010.07.008.
Pascal, C., Cloetingh, S.A.P.L., 2002. Rifting in heterogeneous lithosphere: inferences from numerical modeling of the northern north sea and the oslo graben. Tectonics 21, 1–10. http://dx.doi.org/10.1029/2001TC901044.
Peltonen, P., Brügmann, G., 2006. Origin of layered continental mantle (karelian craton, finland): geochemical and re-os isotope constraints. Lithos 89, 405–423. http://dx.doi.org/10.1016/j.lithos.2005.12.013.
Polat, A., Kusky, T., Li, J., Fryer, B., Kerrich, R., Patrick, K., 2005. Geochemistry of neoarchean (ca. 2.55?2.50 ga) volcanic and ophiolitic rocks in the Wutaishan Greenstone Belt, Central Orogenic Belt, North China Craton: implications for geodynamic setting and continental growth. Geol. Soc. Am. Bull. 117, 1387–1399. http://dx.doi.org/10.1130/B25724.1.
Poli, S., Schmidt, M.W., 2002. Petrology of subducted slabs. Annu. Rev. Earth Planet. Sci. 30, 207–235. http://dx.doi.org/10.1146/annurev.earth.30.091201.140550.
Ranalli, G., 1995. Rheology of the Earth. Chapman & Hall, London, UK.
Romanowicz, B., 2009. The thickness of tectonic plates. Science 324, 474–476. http://dx.doi.org/10.1126/science.1172879.
Rychert, C.A., Shearer, P.M., 2009. A global view of the lithosphere–asthenosphere boundary. Science 324, 495–497. http://dx.doi.org/10.1126/science.1169754.
Schenker, F.L., Gerya, T., Burg, J.P., 2012. Bimodal behavior of extended continental lithosphere: modeling insight and application to thermal history of migmatitic core complexes. Tectonophysics 579, 88–103. http://dx.doi.org/10.1016/j.tecto.2012.07.002.
Schmidt, M.W., Poli, S., 1998. Experimentally based water budgets for dehydrating slabs and consequences for arc magma generation. Earth Planet. Sci. Lett. 163, 361–379.
Sleep, N., 2009. Stagnant lid convection and carbonate metasomatism of the deep continental lithosphere. Geochem. Geophys. Geosyst. 10, 1–16. http://dx.doi.org/10.1029/2009GC002702.
Tappe, S., Foley, S.F., Stracke, A., Romer, R.L., 2007. Craton reactivation on the Labrador Sea Margins: 40AR/39AR age and Sr–Nd–Hf–Pb isotope constraints from alkaline and carbonatite intrusives. Earth Planet. Sci. Lett. 256, 433–454. http://dx.doi.org/10.1016/j.epsl.2007.01.036.
Thybo, H., 2006. The heterogeneous upper mantle low velocity zone. Tectonophysics 416, 53–79. http://dx.doi.org/10.1016/j.tecto.2005.11.021.
Thybo, H., Perchuc, E., 1997. The seismic 8° discontinuity and partial melting in continental mantle. Science 275, 1626–1629.
Turcotte, D.L., Schubert, G., 2002. Geodynamics. Cambridge University Press, Cambridge, UK.
Vauchez, A., Barruol, G., Tommasi, A., 1997. Why do continents break-up parallel to ancient orogenic belts? Terra Nova 9, 62–66.
Wang, Q., 2010. A review of water contents and ductile deformation mechanisms of olivine: implications for the lithosphere–asthenosphere boundary of continents. Lithos 120, 30–41. http://dx.doi.org/10.1016/j.lithos.2010.05.010.
Xu, Y.G., 2001. Thermo-tectonic destruction of the Archaean lithospheric keel beneath the Sino-Korean Craton in China: evidence, timing and mechanism. Phys. Chem. Earth 26, 747–757.
Xu, W., Hergt, J.M., Gao, S., Pei, F., Wang, W., Yang, D., 2008. Interaction of adakitic melt-peridotite: implications for the high-mg signature of mesozoic adakitic rocks in the eastern North China Craton. Earth Planet. Sci. Lett. 265, 123–137. http://dx.doi.org/10.1016/j.epsl.2007.09.041.
Xu, Y., Li, H., Pang, C., He, B., 2009. On the timing and duration of the destruction of the North China Craton. Chin. Sci. Bull. 54, 3379–3396. http://dx.doi.org/10.1007/s11434-009-0346-5.
Yoshida, M., 2012. Dynamic role of the rheological contrast between cratonic and oceanic lithospheres in the longevity of cratonic lithosphere: a three-dimensional numerical study. Tectonophysics 532–535, 156–166. http://dx.doi.org/10.1016/j.tecto.2012.01.029.
Yuan, H., Romanowicz, B., 2010. Lithospheric layering in the North American Craton. Nature 466, 1063–1069. http://dx.doi.org/10.1038/nature09332.
Zhang, Z., Wu, J., Y. D., Teng, J., Zhang, X., Chen, Y., Panza, G., 2012. Lateral variation of the strength of lithosphere across the eastern North China Craton: new constraints on lithospheric disruption. Gondwana Res. 22, 1047–1059. http://dx.doi.org/10.1016/j.gr.2012.03.006.
Zhao, l, Xue, M., 2010. Mantle flow pattern and geodynamic cause of the North China Craton reactivation: evidence from seismic anisotropy. Geochem. Geophys. Geosyst. 11, 1–18. http://dx.doi.org/10.1029/2010GC003068.
Zheng, T., Zhao, L., Zhu, R., 2009. New evidence from seismic imaging for subduction during assembly of the North China Craton. Geology 37, 395–398. http://dx.doi.org/10.1130/G25600A.1.
Zuber, M.T., Parmentier, E.M., 1986. Lithospheric necking: a dynamic model for rift morphology. Earth Planet. Sci. Lett. 77, 373–383.